

Article

The Formation of Composite Ti-Al-N Coatings Using Filtered Vacuum Arc Deposition with Separate Cathodes

Ivan A. Shulepov ¹, Egor B. Kashkarov ^{1,*} , Igor B. Stepanov ¹, Maxim S. Syrtanov ¹, Alina N. Sutygina ¹, Ivan Shanenkov ¹, Aleksei Obrosov ²  and Sabine Weiß ² 

¹ Department of General Physics, National Research Tomsk Polytechnic University, Tomsk 634050, Russia; shulepovia@tpu.ru (I.A.S.); stepanovib@tpu.ru (I.B.S.); maxim-syrtanov@mail.ru (M.S.S.); sutygina2013@mail.ru (A.N.S.); swordi@list.ru (I.S.)

² Physical Metallurgy and Materials Technology, Brandenburg Technical University, 03046 Cottbus, Germany; aleksei.obrosov@b-tu.de (A.O.); sabine.weiss@b-tu.de (S.W.)

* Correspondence: egor_kashkarov@mail.ru; Tel.: +7-952-802-0688

Received: 15 October 2017; Accepted: 7 November 2017; Published: 12 November 2017

Abstract: Ti-Al-N coatings were deposited on high-speed steel substrates by filtered vacuum arc deposition (FVAD) during evaporation of aluminum and titanium cathodes. Distribution of elements, phase composition, and mechanical properties of Ti-Al-N coatings were investigated using Auger electron spectroscopy (AES), X-ray diffraction (XRD), transmission electron microscopy (TEM) and nanoindentation, respectively. Additionally, tribological tests and scratch tests of the coatings were performed. The stoichiometry of the coating changes from $Ti_{0.6}Al_{0.4}N$ to $Ti_{0.48}Al_{0.52}N$ with increasing aluminum arc current from 70 A to 90 A, respectively. XRD and TEM showed only face-centered cubic Ti-Al-N phase with preferred orientation of the crystallites in (220) direction with respect to the sample normal and without precipitates of AlN or intermetallics inside the coatings. Incorporation of Al into the TiN lattice caused shifting of the (220) reflex to a higher 2θ angle with increasing Al content. Low content and size of microdroplets were obtained using coaxial plasma filters, which provides good mechanical and tribological properties of the coatings. The highest value of microhardness (36 GPa) and the best wear-resistance were achieved for the coating with higher Al content, thus for $Ti_{0.48}Al_{0.52}N$. These coatings exhibit good adhesive properties up to 30 N load in the scratch tests.

Keywords: filtered vacuum arc; deposition; TiAlN; separate cathodes; phase composition; hardness; wear-resistance

1. Introduction

Wear-resistant coatings based on transition metal nitrides are an effective way to increase the resistance of cutting tools. Various studies have noted an increase in wear-resistance up to tenfold. Binary systems such as TiN are the most frequently studied wear-resistant coatings [1]. Ti-Al-N coatings are designed to improve the functional characteristics of TiN such as hardness, friction coefficient, high temperature oxidation and chemical stability [2–6]. The widespread technologies for super-hard wear-resistant coatings are based on evaporation of materials in a vacuum, the so called physical vapor deposition (PVD). Among the various PVD technologies, the vacuum-arc deposition (VAD) method is the most frequent application for Ti-Al-N coating deposition [7–10]. In addition, VAD is the main method for deposition of transition metal nitrides due to its high degree of ionization, high-energy particles (50–100 eV) and deposition rate as well as the wide range of cathode materials. Furthermore, evaporated coatings exhibit higher density and adhesion than sputtered coatings [11].

The resistance of cutting tool edges with coating depends on different factors including the crack formation. Initiation and propagation of cracks both start from the cutting edge and the tool body.

Efficiency and crack resistance of a tool can be increased by deposition of multilayer coatings [12,13]. Therefore, different chemical compositions of layers decelerate crack formation, increase the adhesion to the tool body surface, and reduce the thermal conductivity in the direction of the tool [14].

However, a large number of microdroplets is formed on the material surface during deposition of the coatings by conventional vacuum-arc systems. These microdroplets lead to a degradation of the mechanical properties of the coatings as well as the appearance of pores formed by the merger of micro-particles emitted from the cathode [15]. In this study, a decrease of microdroplet fraction was reached using a shutter type coaxial plasma filter. Usually Ti-Al-N coatings are deposited using TiAl composite cathodes with different Ti/Al ratio. However, the use of separate cathodes permits better control of the coating composition as a result of changing the Ti/Al ratio.

Thus, the aim of this work is to investigate phase-and elemental composition of Ti-Al-N coatings fabricated by filtered vacuum arc deposition using separate aluminum and titanium cathodes. Subsequently mechanical and tribological properties of the deposited coatings were analyzed.

2. Experimental Procedure

2.1. Substrate Preparation

Discs with diameter of 40 mm and thickness of 3 mm were cut from R6M5 HSS rods (BSM, Novosibirsk, Russia); (0.82–0.9% C, 0.2–0.5% Si, 0.2–0.5% Mn, 0.6% Ni, 0.03% P, 0.025% S, 3.8–4.4% Cr, 4.8–5.3% Mo, 5.5–6.5% W, 1.7–2.1% V, 0.5 % Co, 0.25% Cu, Fe balance, in wt %). The heat treatment was performed according to the technology of cutting tool production. The sample surface was ground and polished in the grinding-polishing machine Saphir 320 E (Advanced Materialography, Germany) to a final roughness of $R_a = 0.04 \mu\text{m}$. The deviation from the plane was 0.5–1 μm . The samples were cleaned with alcohol prior to installation into the chamber.

2.2. Ti-Al-N Coatings Deposition

Ti-Al-N coatings were deposited by VAD Rainbow-5 (National Research Tomsk Polytechnic University, Tomsk, Russia), using the experimental technique shown in Figure 1. The plasma generator was installed in the upper part of the vacuum chamber. The plasma gas flow is formed by a non-sustaining arc discharge with a glowing cathode. The plasma generator is implemented reactive gas inlet system through the cathode. The experimental setup was equipped with a coaxial plasma filter (PF) to clean the plasma flow from microdroplets [16,17].

Recently, the most effective and typically used plasma filtering systems are based on the principle of separation of ion flow from the plasma. The most commonly used vacuum arc deposition system equipped with large 90° rectangular duct filters. The plasma filter used in this paper based on the principle of avoiding line-of-sight between cathode and substrate. The efficiency of plasma transmission through this filter could be more than 30% [18]. Similarly principle also used in Venetian Blind Filters, where the plasma transmission ratio of 20% has been achieved [19,20]. The PF is a set of nested conical electrodes. Shape and angle of inclination relative to the axis provide optical opaqueness of the filter from all points on the cathode surface. The electrodes are made of copper tubes to ensure water cooling and to avoid overheating of the working surface of the filter. The second-order surfaces of the electrodes optimize the filter transparency. The operation principle of the filter is based on creating a magnetic field close to the electrodes. A positive bias voltage of 10–15 V is applied to the electrodes to increase the filter transparency for plasma flow due to deflection of the ions from the electrodes.

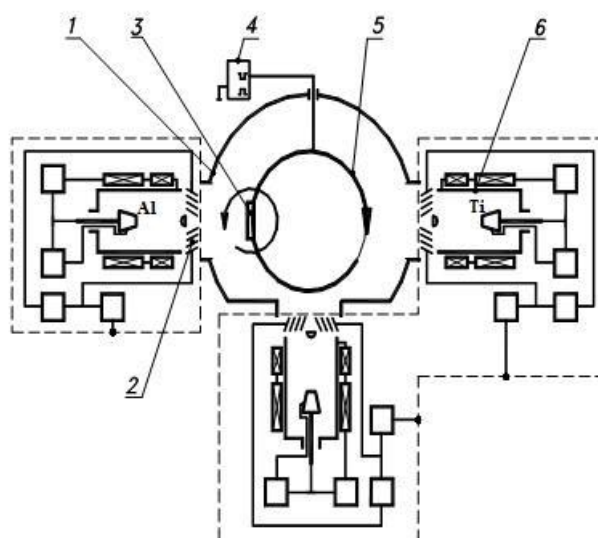


Figure 1. Schematic diagram of the experimental technique: 1—vacuum chamber; 2—plasma filter; 3—sample; 4—bias voltage supply; 5—rotary device; 6—arc evaporator.

The filter system is placed close to the arc evaporator. The bias voltage supply is equipped with automatic arc suppression system and protection device against overvoltage occurring at the arc extinction. The temperature of the samples was monitored using a pyrometer. Basic technical characteristics of the experimental setup are shown in Table 1.

Table 1. Experimental setup characteristics.

Arc evaporator	
Arc current, A	40–250
Plasma concentration, cm^{-3}	$\leq 4 \times 10^{10}$
Plasma flow diameter, mm	200
Gas plasma generator	
Operation pressure, Pa	10^{-2} –1
Plasma concentration, cm^{-3}	10^9 – 10^{11}
Discharge current, A	5–150

During deposition the samples were rotated around their axis (0.5 s^{-1}) and the center of the chamber (0.1 s^{-1}). The samples were placed in a distance of 200 mm from the plasma filter. Initial cleaning and heating of the samples were performed inside the vacuum chamber using the low temperature nitrogen plasma at a pressure of 10^{-1} Pa. The negative bias potential (U_b) of 1200 V was applied to the samples. The sample temperature was maintained in the range of 360–400 °C. Subsequently, the surface of samples was treated under the joint influence of nitrogen and titanium plasma flows. The bias voltage was kept constant at 1200 V. Considering the charge state of the ions, the impact of the prevailing process on the surface was ion etching accompanied by the formation of a large number of active sorption sites as well as sample heating between 360 °C and 400 °C. Finally, the bias voltage was reduced to 150 V when formation of the interlayer and coating deposition in the ion assisting mode become the prevailing processes. The temperature of the samples increases to 400–420 °C. The total pressure in the vacuum chamber was 5×10^{-3} Pa. The ratio of Ti and Al plasma flows was determined by the arc current (I). Coating deposition was carried out at constant $I_{\text{Ti}} = 120$ A and $I_{\text{Al}} = 70, 80, 90$ A.

2.3. Characterization

The depth distribution profiles of the elements were measured using Auger electron spectroscopy. The energy resolution of Auger electrons was 0.5–0.7%. The energy of the electron probe beam and the beam diameter were 3 keV and $\sim 1 \mu\text{m}$, respectively. The surface sputtering was carried out by argon ions with 3 MeV energy and 1 mm beam diameter. The axis inclination of the ion beam was 20° relative to the surface of the sample.

The nanohardness of the coatings was measured using a nanohardness tester NHT-S-AX-000X (CSEM, Neuchatel, Switzerland). This device analyzes load changes and indenter penetration depth at the loading-unloading cycle. A load of 10 mN was used, hence the penetration depth did not exceed 1/10th of the coating thickness to avoid the substrate effect. An average value of 10 measurements was considered for each film. Wear resistance and friction coefficients were investigated using a high-temperature tribometer TNT-S-AH0000 (CSEM, Neuchatel, Switzerland) and a Micro-Scratch Tester MST-S-AX-0000 (CSEM, Neuchatel, Switzerland). A special feature is scratching the surface of the sample by applying a progressive load to the spherical diamond indenter. As a result, the wear resistance can be determined by analyzing the longitudinal scratch area.

The phase composition of the coatings was investigated by carbon extraction replicas using transmission electron microscope (TEM) (JEOL JEM-2100 (JEOL, Tokyo, Japan) with accelerating voltage of 125 kV. Initially, the coatings were pricked with the hardness tester indenter. Subsequently, amorphous graphite was deposited on top of the film. Finally, graphite film and coatings were detached from the sample and placed on the sample holder of the electron microscope. The analyzed area was approximately one micrometer. Phase identification and structural investigations were performed by X-ray diffraction with $\text{CuK}\alpha$ radiation (1.5410 \AA wavelength) using a Shimadzu XRD-7000 diffractometer (Shimadzu, Kyoto, Japan) in Bragg-Brentano geometry at 40 kV and 30 mA.

The Raman spectra of the coatings were studied using the complex correlator of the optical, spectral and topographic properties of the surface Centaur HR (Nano ScanTechnologies, Moscow, Russia). The optical wavelength of the laser was $\lambda = 532 \text{ nm}$. The data were collected with data point acquisition time of 180 s in the spectral region of $200\text{--}800 \text{ cm}^{-1}$.

3. Results and Discussion

3.1. Elemental and Phase Composition

Figure 2 shows the Auger spectra of the samples registered in a depth of 20–30 nm. The main peaks of Al, Ti, O and impurities (Ar, C) are observed. Shape and position of the Ti + N peak (383 eV) show the existence of Ti-N bonds for all deposited coatings [21]. The presence of Auger electrons with the energy of Al₁-52 eV and Al-68 eV demonstrate the different chemical bonds of aluminum. The intensity of the Al₁ peak (52 eV) corresponds to Al-O bonds in Al₂O₃ slightly decreasing with increasing Al content in the Ti-Al-N coating [22]. This suggests that oxygen from the residual atmosphere binds to aluminum, while the Al-O bonds are reduced with increasing aluminum arc current. Another Al peak (68 eV) is attributed to metallic Al or Al-N bonds in AlN [21]. Nitrogen has a tendency to react with Ti or Al, because of the negative free energy of formation for both ($\Delta G_0(\text{TiN}) = -308.3 \text{ kJ}\cdot\text{mol}^{-1}$, $\Delta G_0(\text{AlN}) = -287.0 \text{ kJ}\cdot\text{mol}^{-1}$). Thus, the increasing intensity of Al-68 eV is related to the increase of aluminum in the coating, which is bonded with nitrogen. The formation of Al-N bonds is clearly visible at higher Al cathode currents of 80 A and 90 A when the stoichiometry of the coatings is Ti_{0.57}Al_{0.43}N and Ti_{0.48}Al_{0.52}N, respectively. According to the AES spectra the stoichiometry of the coating deposited at lower Al cathode current was Ti_{0.6}Al_{0.4}N. The colors of coatings change towards golden-brown (70 A), reddish-brown (80 A) and grey (90 A) with increasing Al content reported in [23] too. Despite the increase in Al concentration inside the Ti-Al-N coating accompanied by the appearance of Al-N bonds, Ti-N remains the main bond for all deposition parameters.

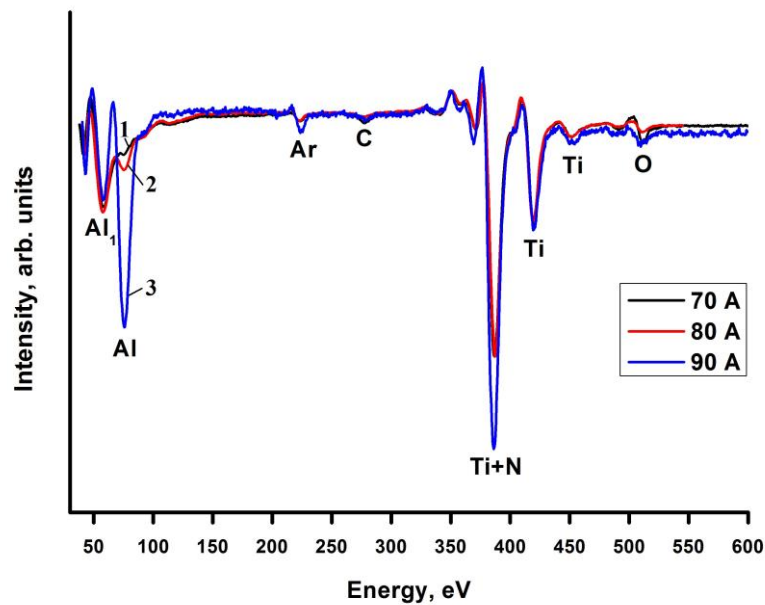


Figure 2. Auger electron spectroscopy (AES) of Ti-Al-N coatings at I_{Al} : 1–70 A; 2–80 A; 3–90A.

Figure 3 shows the element distribution obtained by Auger profiling. The concentration of aluminum inside the Ti-Al-N coating increases from 22 to 37 at % with increasing Al cathode current. The corresponding stoichiometry of the coatings is shown above. The presence of interlayers between substrate and coating may indicate that due to ion assisting an intense diffusion process near the surface of the samples is stimulated. There is a uniform distribution of elements over the thickness of the coatings. However, surface and interface of the sample deposited at 70 A contain higher concentration of oxygen than the ones deposited at 80 and 90 A. In this case, the presence of Al-O bonds of Al_2O_3 is clearly documented by the AES spectra (Figure 2). The thicknesses of the coatings were approx. 580 nm, 750 nm and 1200 nm for 70, 80 and 90 A aluminum cathode currents.

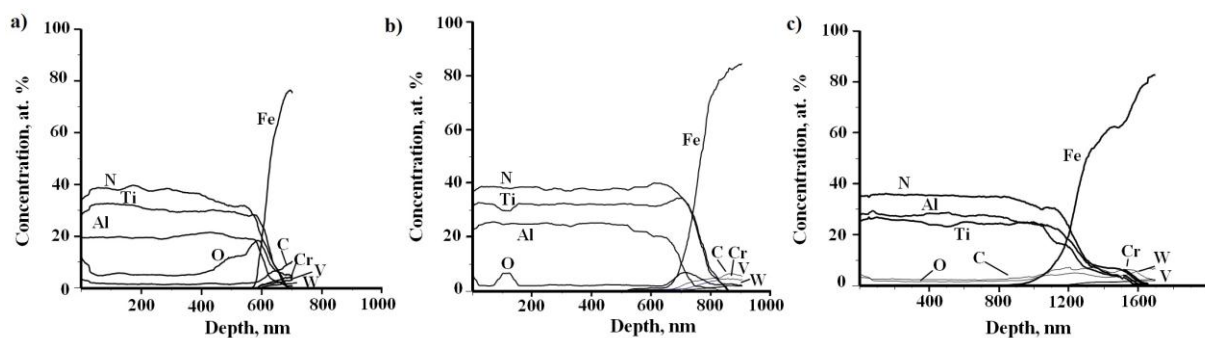


Figure 3. AES distribution profiles of elements in the samples deposited at I_{Al} : 70 A (a); 80 A (b); 90 A (c).

Figure 4 shows X-ray diffraction patterns of Ti-Al-N coatings on the HSS substrates. The analysis of all samples revealed the presence of alpha iron α -Fe, iron-tungsten nitride Fe_4W_2N and face-centered cubic (fcc) titanium-aluminum nitride $Ti_xAl_{1-x}N$ phases. The HSS substrate is represented by two phases—the main phase corresponds to cubic Fe and the other phase corresponds to Fe_4W_2N nitride formed during preliminary plasma etching. There is no diffraction reflex of titanium-aluminum nitride phase within the the reflexes of the (111) and (200) planes indicating that (220) is the preferred orientation of the films. For Ti-Al-N films with fcc structure, (111) is the densest packed plane, while films with (220) preferred orientation have the lowest strain energy [24].

Formation of the complex nitride $Ti_xAl_{1-x}N$ and shifting of the (220) reflection to a higher 2θ angle with increasing Al content inside the coating are caused by substitution of Ti atoms by Al atoms inside the TiN lattice, where Al atoms bonded to N form AlN resulting in the solid solution Ti-Al-N phase. The increase in the intensity of (220) reflection with increasing cathode current is associated with the higher coating thickness. The average crystallite size of the regions of coherent scattering was determined by the Scherrer equation from the broadening of the diffraction peaks [25,26]. For the Ti-Al-N phase, the crystallite size ranges from 8 nm to 10 nm indicating its nanocrystalline structure.

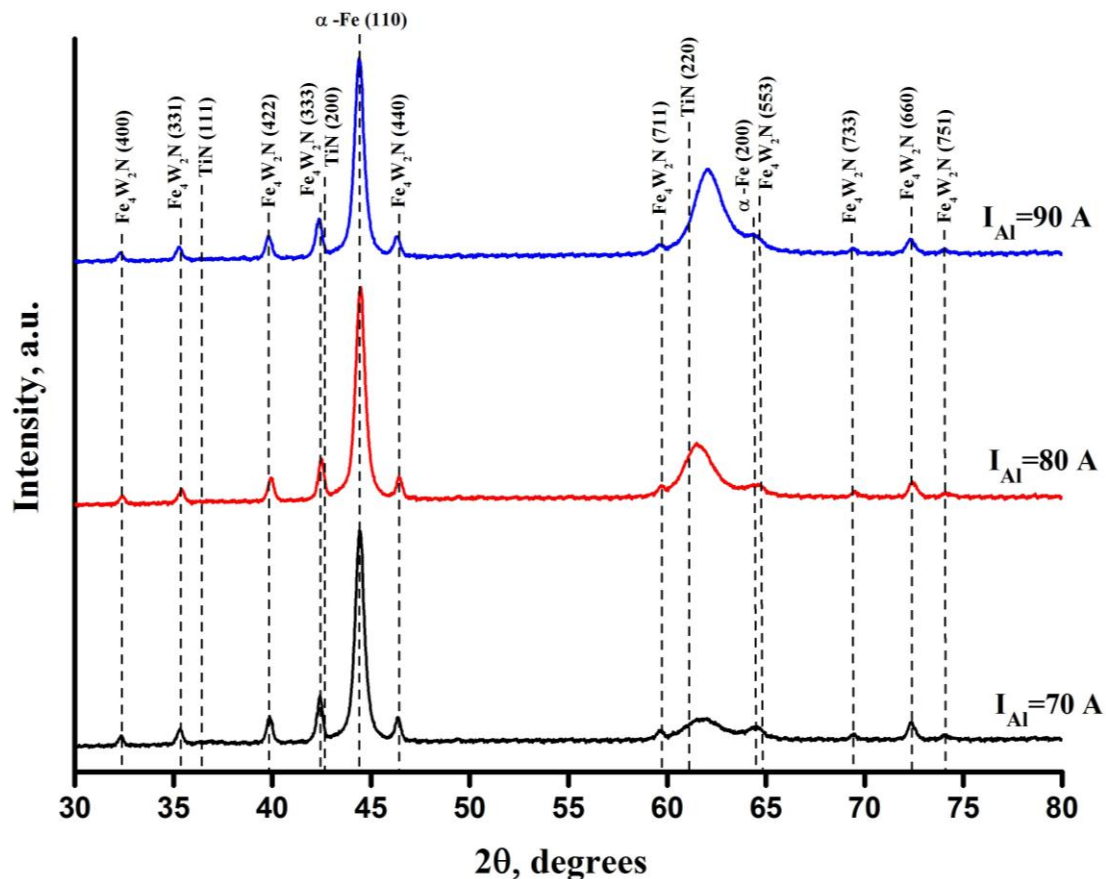


Figure 4. X-ray diffraction (XRD) analysis of Ti-Al-N coatings.

Figure 5 shows surface morphology (SEM image) and microstructure (TEM image) of the coating deposited at 90 A combined with dark field imaging and selected area electron diffraction (SAED) pattern. The surface is covered uniformly by the coating without any cracks or peelings (Figure 5a). The visible traces are formed after sample polishing. Isolated microparticles with a size up to 3–5 μm are observed. The microparticles appeared during evaporation of material in the cathodic spots [27]. Reducing the amount of microparticles on the surface which negatively affect the mechanical and tribological properties of Ti-Al-N coatings is still of particular interest. A large number of microparticles are formed during evaporation of the aluminum cathode due to the low melting point of aluminum. However, the shutter-type plasma filters used in this work significantly reduce the amount of microparticles on the surface, in particular those of aluminum, whose size could reach 20 μm or more in diameter without any filter systems.

The SAED pattern confirmed the fcc structure of Ti-Al-N and the random orientation of the crystallites as well as the absence of any noticeable precipitates, such as AlN-phases. For all deposited Ti-Al-N coatings, cubic c-TiAlN phase is formed. The obtained coatings are finely dispersed and form a homogeneous nanostructure with crystallite sizes of only few nanometers.

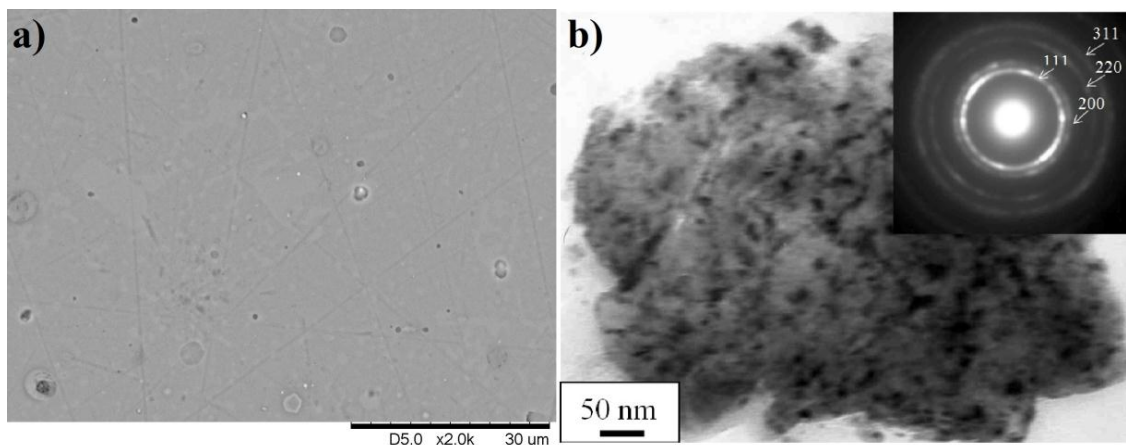


Figure 5. Surface scanning electron microscopy (SEM) image (a), and transmission electron microscopy (TEM) micrograph (b), of Ti-Al-N coating deposited at 90 A.

3.2. The Mechanical and Tribological Properties

Figure 6 shows that hardness and elastic modulus of Ti-Al-N coatings were influenced by the aluminum cathode arc currents. The hardness and E-modulus values rapidly rose from 22.5 ± 0.8 GPa to 36 ± 4 GPa and from 285 ± 15 GPa to 395 ± 45 GPa, respectively, when the aluminum cathode arc currents increased from 70 A to 90 A. Thus, the nanohardness of the coating increases with increasing Al content inside Ti-Al-N. The higher hardness and E-modulus of the $\text{Ti}_{0.48}\text{Al}_{0.52}\text{N}$ coating could observe due to increased levels of microstrains inside the coating and decreased grain size with the addition of aluminum into the TiN lattice. The nanoindentation results are reliable with previous published works by different groups, where the hardness values in the range between 13 and 40 GPa and elastic modulus between 240 GPa and 500 GPa were reported [28–31]. Shum et al. measured hardness and elastic modulus at different deposition condition and found the highest hardness of approximately 31 GPa and elastic modulus of 315 GPa at Al content of 41% [32]. He et al. [31] found that the nanohardness value of the (Ti,Al)N coatings with various Al/Ti atomic ratio were between 30.0 ± 2.0 GPa and 33.4 ± 1.5 GPa, whereas E-Modulus remains stable at 310 ± 25 GPa.

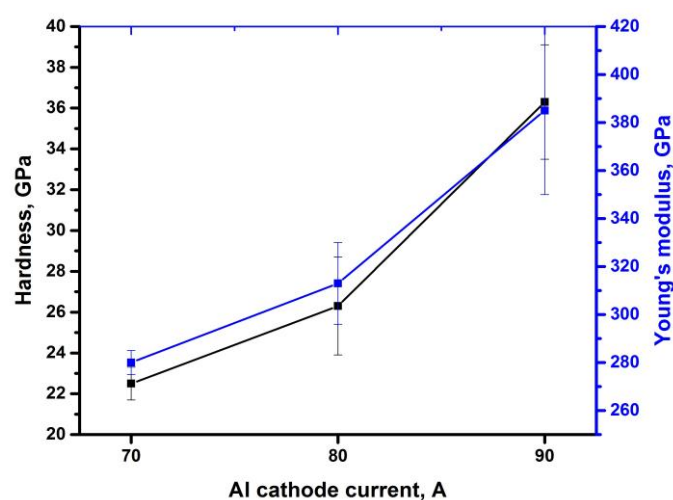


Figure 6. Hardness and Young's modulus of the deposited coatings.

The friction tests were carried out under dry friction conditions with a vertical load of 5 N at a linear sliding speed of 2.5 cm/s for 15000 laps (the distance is approx. 150 m). The results (Figure 7)

indicate that the highest friction coefficient (COF) of (0.20 ± 0.03) is measured for Ti-Al-N deposited at the arc current $I_{Al} = 70$ A and the lowest is (0.17 ± 0.02) for $I_{Al} = 80$ A. Insignificant fluctuations in COF values were observed for the sample deposited at the arc current of 90 A (0.18 ± 0.01). The strong changes in COF for the deposited coatings in the initial stage are characterized by ploughing friction arising from micro surface asperities. Small powder-like particles are generated from the wear debris after the initial stage of sliding. The entrapped hard wear particles can cause a ploughing friction and negligible interlocking effects can occur. However, at the end of the test (more than than 7000 laps), accumulation and entrapment of large wear particles are initiated. By increasing quantity and size of the wear particles, the friction behavior due to third-body hard particles is ploughing [33,34]. Therefore, fluctuations and rapid increase in friction coefficient at the end of the test occur. Moreover, the fluctuations in COF can be explained by the fact that microdroplets adhere or stick on the SiC ball, which are detached and removed mechanically. The samples have different aluminum concentration within the coating, which influences the behavior of the friction coefficient. The difference between the COFs is not significant; however, the deposited coatings have very low COF values for TiAlN, generally achieved by the addition of different elements [35,36]. Typical COFs for Ti-Al-N coatings vary from 0.4 to 0.8 [37–39].

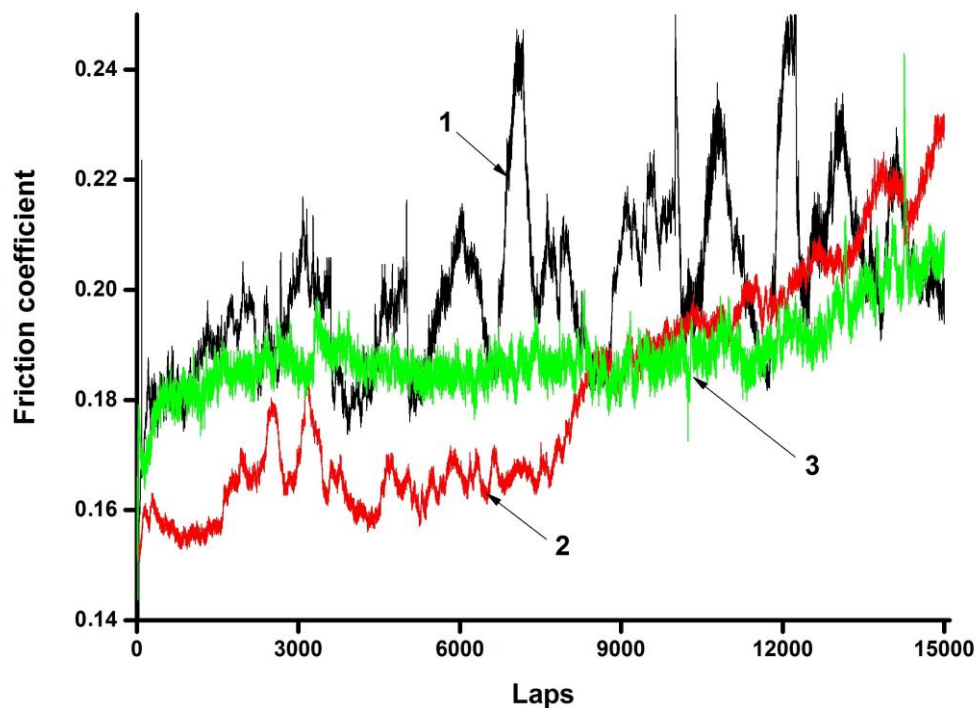


Figure 7. Friction coefficient evolution of Ti-Al-N coatings deposited at I_{Al} : 1–70 A; 2–80 A; 3–90 A.

The Raman spectra of the as-deposited coatings (a) and the tracks after tribological tests (b) are shown in Figure 8. The Raman spectrum of Ti-Al-N coatings is mainly determined by the vibrations of the heavy metal ions (typically $150\text{--}350\text{ cm}^{-1}$) and in the optic range by the vibrations of the lighter N ions (typically $550\text{--}650\text{ cm}^{-1}$) [40,41]. Two bands centered at ~ 225 and $\sim 310\text{ cm}^{-1}$ corresponding to longitudinal and transversal acoustic (LA and TA) modes and one broad band at 560 cm^{-1} (LO and TO modes) are observed for the Ti-Al-N coating deposited at $I_{Al} = 70$ A (Figure 8a). Substitution of Ti atoms by Al atoms in TiN matrix affects the Raman spectra at $I_{Al} = 90$ A, where only two broad bands centered at 256 cm^{-1} (LA and TA) and 657 cm^{-1} (LO and TO) are observed. The shifting of bands to higher values with increasing Al content is caused by incorporation of Al into the TiN lattice. No signatures of pure AlN, Al_2O_3 and TiO_2 phases were seen in the Raman spectrum after tribological testing (Figure 8b), indicating absence of these phases inside the tracks. Nevertheless, for the Ti-Al-N

film with higher Al concentration ($I_{Al} = 90$ A), the bands at 700 cm^{-1} are significantly higher than the typical vibrations in the optic range for Ti-Al-N that could be attributed to the oxidation of Al during wear. Aluminum atoms on the surface are prone to oxidation forming Al_2O_3 oxide with self-lubricating character, which reduces friction coefficient and wear of the coating [23,42].

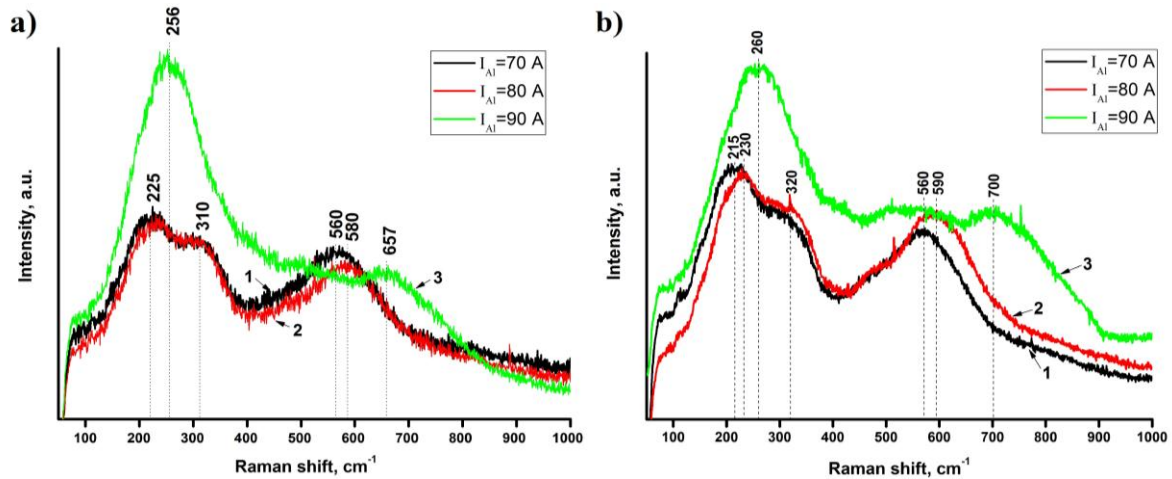


Figure 8. Raman spectra of deposited Ti-Al-N coatings obtained on the surface (a) and inside the wear track (b).

The adhesion of the coatings on the HSS substrates was analyzed by the scratch method using a Rockwell indenter with progressive load up to 30 N (Figure 9). The Ti-Al-N coatings deposited at the arc currents 80 A and 90 A show minor damages in comparison with the coating of the sample deposited at 70 A arc current. It can be concluded that there is a strong bond between the coatings and the HSS substrates. Figure 9 shows numerous chippings of the coatings at the border of the sliding indenter, which can be related to cracks formed during indenter penetration and plastic deformation of the substrate. The lightest areas within the scratches are attributed to the mashed aluminum microdroplets formed as a result of cathodic arc evaporation [27,43]. A partial removing of the coating at 26 N applied load is observed only exclusively for the Ti-Al-N coating deposited at the arc current 70 A (Figure 9a). Otherwise, the coatings deposited at the higher arc currents remain on the substrate surface up to 30 N load, while semicircular transverse cracks are initiated under loads of 26 N (80 A) and 24 N (90 A) (Figure 9e,h), respectively.

The hard and thin coatings demonstrate good adhesion and cohesion properties, which are characterized by only small radial cracks and no spalling of the coating in the scratch area.

Figure 10 shows the average area after three scratch tests for each sample measured by a profilometer, which provides important information about wear resistance of the coatings as well as the coefficient of friction. The average wear area for the TiAlN coated HSS at 70, 80 and 90 A arc currents are $(7.5 \pm 0.5) \times 10^3$, $(6.7 \pm 0.4) \times 10^3$ and $(5.1 \pm 0.2) \times 10^3\ \mu\text{m}^2$, respectively. The average scratching area decreases gradually with increasing arc current, which reflecting an enhancement in the wear resistance values with increasing aluminum content inside the coating. These results are in good agreement with the COFs and the scratch morphology discussed above (Figures 8 and 9). The coating thickness increases with the arc current. The decrease in coating thickness during the wear process leads to a reduction of the combined hardness and the load-bearing capability of the coatings declines [43–45]. Most existing wear data for Ti-Al-N coatings are presented for (111) oriented coatings since it is the general growth direction produced by cathodic arc deposition with dc bias. Many studies in the literature focus on wear behavior of TiN and Ti-Al-N with different orientations of the coatings [46,47]. However, the wear behavior is mostly documented for (111) and (200) oriented coatings without indicating the influence of preferred orientation on the wear behavior. To the authors

best knowledge no studies on the wear behavior of highly (220) oriented Ti-Al-N films deposited using filtered vacuum arc exist. The preferred (220) orientation of the coatings could affect the wear resistance [48] positively, since the elastic moduli of (220) planes are higher than the ones of (111) oriented planes [49].

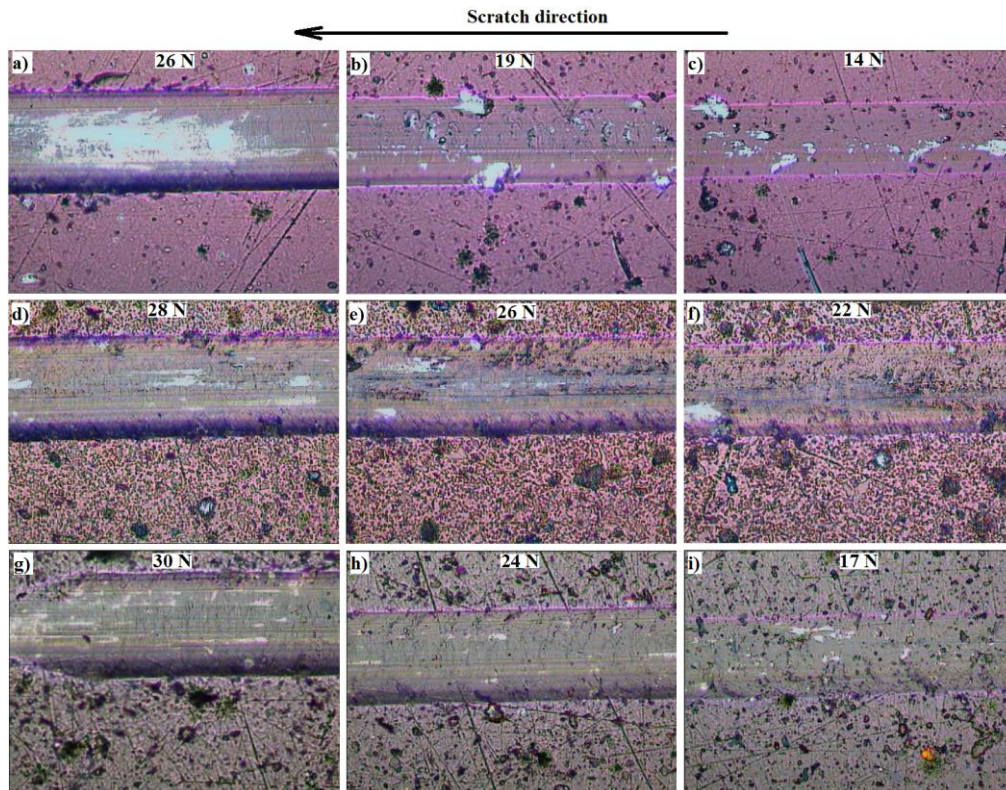


Figure 9. Scratches of the samples deposited at I_{Al} : 70 A (a–c); 2–80 A (d–f); 3–90 A (g–i).

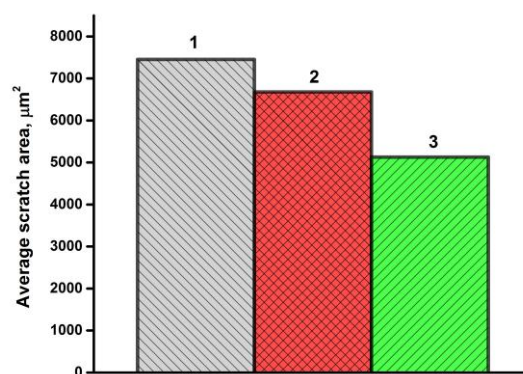


Figure 10. Schematic diagram shows the average scratching area at different arc currents: 1— I_{Al} = 70 A; 2— I_{Al} = 80 A; 3— I_{Al} = 90 A.

4. Conclusions

Ti-Al-N coatings were deposited by filtered VAD with separate Ti and Al cathodes. Different arc currents were applied on the Al cathode. The stoichiometry of the coatings changes from $\text{Ti}_{0.6}\text{Al}_{0.4}\text{N}$ to $\text{Ti}_{0.48}\text{Al}_{0.52}\text{N}$ with increasing aluminum arc current from 70 to 90 A. All deposited coatings exist in the form of fcc Ti-Al-N phase with preferred orientation of crystallites in (220) direction. Incorporation of Al atoms into the TiN lattice is observed with increasing Al content inside the coating. The coatings

exhibit good mechanical and tribological properties that are strongly influenced by Al content and preferred (220) texture. Simultaneous cleaning and nitriding of the surface occurs during preliminary ion cleaning of HSS in the nitrogen plasma leading to a nitride interlayer composed of $\text{Fe}_4\text{W}_2\text{N}$ phase. The coatings deposited under optimum conditions exhibit excellent performance with a high hardness of 36 GPa and a low friction coefficient of 0.18 qualifying them for industrial applications.

Acknowledgments: The research is funded by Governmental program “Science”, research project No.11.3683.2017/4.6 as well as by Tomsk Polytechnic University Competitiveness Enhancement Program grant.

Author Contributions: Igor Stepanov carried out the deposition process. Egor Kashkarov and Ivan Shanenkov analyzed the results and prepared the paper. Aleksei Obrosov provided nanoindentation and described results. Ivan Shulepov provided TEM and AES investigation. Alina Sutygina carried out Raman and tribology. Maxim Syrtanov provided XRD. Sabine Weiß revised the manuscript.

Conflicts of Interest: The authors declare no conflict of interest.

References

- Zhitomirsky, V.N.; Grimberg, I.; Rapoport, L.; Travitzky, N.A.; Goldsmith, S.; Weiss, B.Z. Bias voltage and incidence angle effects on the structure and properties of vacuum arc deposited TiN coatings. *Surf. Coat. Technol.* **2000**, *133–134*, 114–120. [[CrossRef](#)]
- Tonshoff, K.; Mohlfeld, A.; Leyendecker, T.; Fu, H.G.; Erkens, G.; Wenke, R.; Cselte, T.; Schwenck, M. Wear mechanisms of $(\text{Ti}_{1-x}\text{Al}_x)\text{N}$ coatings in dry drilling. *Surf. Coat. Technol.* **1997**, *94–95*, 603–609. [[CrossRef](#)]
- Donohue, L.A.; Smith, I.J.; Munz, W.-D.; Petrov, I.; Greene, J.E. Microstructure and oxidation-resistance of $\text{Ti}_{1-x-y-z}\text{Al}_x\text{Cr}_y\text{Y}_z\text{N}$ layers grown by combined steered-arc/unbalanced-magnetron-sputter deposition. *Surf. Coat. Technol.* **1997**, *94–95*, 226–231. [[CrossRef](#)]
- PalDey, S.; Deevi, S.C. Single layer and multilayer wear resistant coatings of (Ti, Al) N: A review. *Mater. Sci. Eng.* **2003**, *342*, 58–79. [[CrossRef](#)]
- Mayrhofer, P.H.; Hörling, A.; Karlsson, L.; Sjöln, J.; Larsson, T.; Mitterer, C. Self-organized nanostructures in the Ti-Al-N system. *Appl. Phys. Lett.* **2003**, *83*, 2049–2051. [[CrossRef](#)]
- Chen, L. Mechanical properties of (Ti, Al) N monolayer and TiN/(Ti, Al) N multilayer coatings. *Int. J. Refract. Met. Hard Mater.* **2007**, *25*, 72–76. [[CrossRef](#)]
- Lin, K.L.; Hwang, M.Y.; Wu, C.D. The deposition and wear properties of cathodic arc plasma deposition TiAlN deposits. *Mater. Chem. Phys.* **1996**, *46*, 77–83. [[CrossRef](#)]
- Weber, F.R.; Fontaine, F.; Scheib, M.; Bock, W. Cathodic arc evaporation of (Ti, Al) N coatings and (Ti, Al) N/TiN multilayer-coatings-correlation between lifetime of coated cutting tools, structural and mechanical film properties. *Surf. Coat. Technol.* **2004**, *177–178*, 227–232. [[CrossRef](#)]
- Carvalho, N.J.M.; Zoestbergen, E.; Kooi, B.J.; De Hosson, J.Th.M. Stress analysis and microstructure of PVD monolayer TiN and multilayer TiN/(Ti, Al) N coatings. *Thin Solid Films* **2003**, *429*, 179–189. [[CrossRef](#)]
- Bouzakis, K.D.; Michailidis, N.; Skordaris, G.; Bouzakis, E.; Biermann, D.; Saoubi, R.M. Cutting with coated tools: Coating technologies, characterization methods and performance optimization. *CIRP Ann.* **2012**, *61*, 703–723. [[CrossRef](#)]
- Mashiki, T.; Hikosaka, H.; Tanoue, H.; Takikawa, H.; Hasegawa, Y. TiAlN film preparation by Y-shape filtered-arc-deposition system. *Thin Solid Films* **2008**, *516*, 6650–6654. [[CrossRef](#)]
- Chan, K.S.; He, M.Y.; Hutchinson, J.W. Cracking and stress redistribution in ceramic layered composite. *J. Mater. Sci. Eng.* **1993**, *167*, 57–64. [[CrossRef](#)]
- He, M.Y.; Evens, A.G. Crack deflection at an interface between dissimilar elastic materials: Role of residual stresses. *Int. J. Solids Struct.* **1994**, *31*, 3443. [[CrossRef](#)]
- Rodríguez-Barrero, S.; Fernández-Larrinoa, J.; Azkona, I.; Lópezde Lacalle, L.N.; Polvorosa, R. Enhanced Performance of Nanostructured Coatings for Drilling by Droplet Elimination. *Mater. Manuf. Process.* **2016**, *31*, 593–602. [[CrossRef](#)]
- Ho, W.Y.; Hsu, C.H.; Huang, D.H.; Lin, Y.C.; Chang, C.L.; Wang, D.Y. Corrosion behaviors of Cr(N,O)/CrN double-layered coatings by cathodic arc deposition. *Surf. Coat. Technol.* **2005**, *200*, 1303–1309. [[CrossRef](#)]
- Ryabchikov, A.I.; Stepanov, I.B. Investigations of forming metal-plasma flows filtered from microparticle fraction in vacuum arc evaporators. *Rev. Sci. Instrum.* **1998**, *810*, 1–4. [[CrossRef](#)]

17. Stepanov, I.B.; Ryabchikov, I.A.; Shaposhnikov, P.A.; Kurdyukov, D.M. Formation of vacuum-arc plasma flows in optically opaque plasma guides of the shutter type. In Proceedings of the 5th International Conference on Modification of Materials with Particle Beams and Plasma Flows, Tomsk, Russia, 2–7 October 2000.
18. Ryabchikov, A.I.; Ryabchikov, I.A.; Stepanov, I.B.; Sivina, D.O. Recent advances in surface processing with the filtered DC vacuum-arc plasma. *Vacuum* **2005**, *78*, 445–449. [[CrossRef](#)]
19. Bilek, M.M.M.; Anders, A.; Brown, I.G. Characterization of a linear Venetian-blind macroparticle filter for cathodic vacuum arcs. *IEEE Trans. Plasma Sci.* **1999**, *27*, 1197–1202. [[CrossRef](#)]
20. Zimmer, O. Vacuum arc deposition by using a Venetian blind particle filter. *Surf. Coat. Technol.* **2005**, *200*, 440–443. [[CrossRef](#)]
21. Shew, B.-Y.; Huang, J.-L. Quantitative AES investigation of magnetron sputtered Ti-Al-N films. *Surf. Coat. Technol.* **1995**, *73*, 66–72. [[CrossRef](#)]
22. Hofmann, S. *Auger- and X-ray Photoelectron Spectroscopy in Materials Science: A User-Oriented Guide*; Springer International Publishing AG: Berlin, Germany, 2012; p. 528. ISBN 978-3-642-27381-0.
23. Gakovi, B.; Radak, B.; Radu, C.; Zam, M.; Trtica, M.; Petrovi, S.; Mihailescu, I.N. Selective single pulse femtosecond laser removal of alumina (Al₂O₃) from a bilayered Al₂O₃/TiAlN steel coating. *Surf. Coat. Technol.* **2012**, *206*, 5080–5084. [[CrossRef](#)]
24. Zhao, J.P.; Wang, X.; Chen, Z.Y.; Yang, S.Q.; Shi, T.S.; Liu, X.H. Overall energy model for preferred growth of TiN films during filtered arc deposition. *J. Phys. D: Appl. Phys.* **1999**, *30*, 5–12. [[CrossRef](#)]
25. Cullity, B.D. *Elements of X-Ray-Diffraction*, 2nd ed.; Addison Wesley Publishing: New York, NY, USA, 1978; pp. 42–46, ISBN 0-201-01174-3.
26. Hashhash, A.; Kaiser, M. Influence of Ce-Substitution on Structural, Magnetic and Electrical Properties of Cobalt Ferrite Nanoparticles. *J. Electron. Mater.* **2016**, *45*, 462–472. [[CrossRef](#)]
27. Martin, P.J.; Bendavid, A. Review of the filtered vacuum arc process and materials deposition. *Thin Solid Films* **2001**, *394*, 1–14. [[CrossRef](#)]
28. Wang, C.F.; Ou, S.F.; Chiou, S.Y. Microstructures of TiN, TiAlN and TiAlVN coatings on AISI M2 steel deposited by magnetron reactive sputtering. *Trans. Nonferrous Met. Soc. China* **2014**, *24*, 2559–2565. [[CrossRef](#)]
29. Yi, P.; Peng, L.; Huang, J. Multilayered TiAlN films on Ti6Al4V alloy for biomedical applications by closed field unbalanced magnetron sputter ion plating process. *Mater. Sci. Eng. C* **2016**, *59*, 669–676. [[CrossRef](#)] [[PubMed](#)]
30. Yang, Q.; Seo, D.Y.; Zhao, L.R.; Zeng, X.T. Erosion resistance performance of magnetron sputtering deposited TiAlN coatings. *Surf. Coat. Technol.* **2004**, *188–189*, 168–173. [[CrossRef](#)]
31. He, C.; Zhang, J.; Song, G.; Ma, G.; Du, Z.; Wang, J.; Zhao, D. Microstructure and mechanical properties of reactive sputtered nanocrystalline (Ti,Al) N films. *Thin Solid Films* **2015**, *584*, 192–197. [[CrossRef](#)]
32. Shum, P.W.; Li, K.Y.; Zhou, Z.F.; Shen, Y.G. Structural and mechanical properties of titanium–aluminium–nitride films deposited by reactive close-field unbalanced magnetron sputtering. *Surf. Coat. Technol.* **2004**, *185*, 245–253. [[CrossRef](#)]
33. Godet, M. The third-body approach: A mechanical view of wear. *Wear* **1984**, *100*, 437–452. [[CrossRef](#)]
34. Singer, I.L. How Third-Body Processes Affect Friction and Wear. *MRS Bull.* **1998**, *23*, 37–40. [[CrossRef](#)]
35. Tomaszewski, L.; Gulbinski, W.; Urbanowicz, A.; Suszko, T.; Lewandowski, A.; Gulbinski, W. TiAlN based wear resistant coatings modified by molybdenum addition. *Vacuum* **2015**, *121*, 223–229. [[CrossRef](#)]
36. Banerjee, T.; Chattopadhyay, A.K. Structure, mechanical and tribological characterisations of pulsed DC magnetron sputtered TiN-WS_x composite coating. *Vacuum* **2016**, *130*, 93–104. [[CrossRef](#)]
37. Podgornik, B.; Vizintin, J. Tribology of thin films and their use in the field of machine elements. *Vacuum* **2002**, *68*, 39–47. [[CrossRef](#)]
38. Liew, W.Y.H.; Jie, J.L.L.; Yan, L.Y.; Dayou, J.; Sipaut, C.S.; Madlan, M.F.B. Frictional and Wear Behaviour of AlCrN, TiN, TiAlN Single-layer Coatings, and TiAlN/AlCrN, AlN/TiN Nano-multilayer Coatings in Dry Sliding. *Procedia Eng.* **2013**, *68*, 512–517. [[CrossRef](#)]
39. Huang, X.; Etsion, I.; Shao, T. Effects of elastic modulus mismatch between coating and substrate on the friction and wear properties of TiN and TiAlN coating systems. *Wear* **2015**, *338–339*, 54–61. [[CrossRef](#)]
40. Rebouta, L.; Pitães, A.; Andritschky, M.; Capela, P.; Cerqueira, M.F.; Matilainen, A.; Pischow, K. Optical characterization of TiAlN/TiAlON/SiO₂ absorber for solar selective applications. *Surf. Coat. Technol.* **2012**, *211*, 41–44. [[CrossRef](#)]

41. Constable, C.P.; Yarwood, J.; Munz, W.D. Raman microscopic studies of PVD hard coatings. *Surf. Coat. Technol.* **1999**, *116–119*, 155–159. [[CrossRef](#)]
42. Gao, C.K.; Yan, J.Y.; Dong, L.; Li, D.J. Influence of Al₂O₃ layer thickness on high-temperature stability of TiAlN/Al₂O₃ multilayers. *Appl. Surf. Sci.* **2013**, *285*, 287–292. [[CrossRef](#)]
43. Bobzin, K.; Brögelmann, T.; Brugnara, R.H.; Kruppe, N.C. CrN/AlN and CrN/AlN/Al₂O₃ coatings deposited by pulsed cathodic arc for aluminum die casting applications. *Surf. Coat. Technol.* **2015**, *284*, 222–229. [[CrossRef](#)]
44. Takadom, J.; Bennani, H.H. Influence of substrate roughness and coating thickness on adhesion, friction and wear of TiN films. *Surf. Coat. Technol.* **1997**, *96*, 272–282. [[CrossRef](#)]
45. Holmberg, K.; Matthews, A. *Coatings Tribology: Properties, Mechanisms, Techniques and Applications in Surface Engineering*, 2nd ed.; Elsevier: Cambridge, UK, 2009; pp. 154–196, ISBN 9780080931463.
46. Sundgren, J.E. Structure and properties of TiN coatings. *Thin Solid Films* **1985**, *128*, 21–44. [[CrossRef](#)]
47. Kakas, D.; Terek, P.; Miletic, A.; Kovacevic, L.; Vilotic, M.; Skoric, B.; Krumes, D. Friction and wear of low temperature deposited TiN coating sliding in dry conditions at various speeds. *Tehnicki Vjesnic* **2013**, *20*, 27–33.
48. Akkaya, S.S.; Vasyliov, V.V.; Reshetnyak, E.N.; Kazmanli, K.; Solak, N.; Strel'nitskij, V.E.; Urgen, M. Structure and properties of TiN coatings produced with PIII & D technique using high efficiency rectilinear filter cathodic arc plasma. *Surf. Coat. Technol.* **2013**, *236*, 332–340. [[CrossRef](#)]
49. Mukherjee, S.; Prokert, F.; Richter, E.; Moller, W. Intrinsic stress and preferred orientation in TiN coatings deposited on Al using plasma immersion ion implantation assisted deposition. *Thin Solid Films* **2003**, *445*, 48–53. [[CrossRef](#)]



© 2017 by the authors. Licensee MDPI, Basel, Switzerland. This article is an open access article distributed under the terms and conditions of the Creative Commons Attribution (CC BY) license (<http://creativecommons.org/licenses/by/4.0/>).